ACS MATERIALS LETTERS

Cite This: ACS Materials Lett. 2019, 1, 467−475

www.acsmaterialslett.org

Peptide-Modified Electrode Surfaces for Promoting Anion Exchange Ionomer Microphase Separation and Ionic Conductivity

Zihang Su,[†,▽] Subarna Kole,[‡,▽] Leigh C. Harden,[§] Varada M. Palakkal,[‡] ChulOong Kim,[†] Greshma Nair,[∥] Christopher G. Arges,*[,‡] and Julie N. Renner*[,†]

[†]Department of Chemical and Biomolecular Engineering, Case Western University, Cleveland, Ohio 44106, United States

[‡]Cain Department of Chemical Engineering, Louisiana State University, Baton Rouge, Louisiana 70803, United States

[§]Department of Chemical and Biomolecular Engineering, University of Notre Dame, Notre Dame, Indiana 46556, United States

[∥]Nanofabrication Facility, Center for Advanced Microstructures and Devices (CAMD), Louisiana State University, Baton Rouge, Louisiana 70806, United States

Supporting Information

ABSTRACT: **Ionomer binders are critical materials for delivering ions to and from electrocatalyst surfaces in fuel cell and water electrolyzer technologies. Most studies examine these materials as bulk polymer electrolyte membranes, and comparatively little attention has been given to their behavior on electrode surfaces as thin films. This report demonstrates that sequence-defined peptides anchored to electrode surfaces, or the solvent vapor annealing processing, alters the microstructure configuration of anion exchange ionomers (AEIs). It is observed that moderately sized microphase-separated ionic domains of the AEI, obtained either by peptide-modified electrodes or solvent vapor annealing, give rise to a two- to three-fold increase in thin-film in-plane ionic conductivity. Interestingly, the use of peptide-modified electrodes, in conjunction with solvent vapor annealing, yields excessively large ionic grains that compromise ionic conductivity. Overall, the judicious use of sequence-defined peptides adsorbed to electrode surfaces, or solvent vapor annealing, encourage the appropriate microstructures of thin-film AEIs resulting in ameliorated ionic conductivity.**

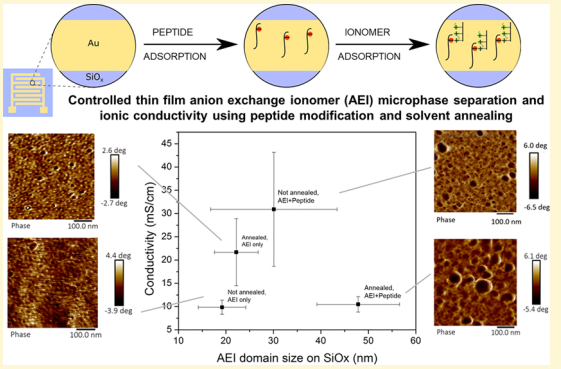

Anion exchange membrane fuel cells and water electrolyzers (AEMFCs and AEMWEs) are modular electrochemical energy storage and conversion technologies that have garnered significant interest as alternatives to commercialized proton exchange membrane devices. The alkaline environment expands the palette of electrocatalyst materials, particularly non-precious group metals, for the necessary redox reactions.[1−6] The electrocatalysts, in many instances, comprise a significant portion of the capital costs of these technologies when manufactured at large volumes.[7−9] Proton exchange membrane fuel cells and water electrolyzers are costly, because of their use of platinum group metals, making widespread proliferation difficult. Their acidic environment restricts the type of electrocatalyst they can use because there are few alternatives to platinum group metals that are both high performing and stable in acid. Alkaline fuel cells and water electrolyzers using a liquid electrolyte are both mature and commercialized technologies that operate effectively with low-cost silver- and nickel-metal-based electrocatalysts,[10−12] but the liquid electrolyte is undesirable, because it can suffer from carbonation, leading to precipitates that clog porous electrodes, and the liquid electrolyte is not conducive to a thin-cell design and may cause shunt currents.[1,13] Hence, AEMFCs and AEMWEs, made possible by anion exchange membranes and ionomers (AEMs and AEIs), offer distinct advantages over liquid alkaline electrolytes and represent a promising pathway to low-cost fuel cell and water electrolyzer technology.

While there are several reviews[1,2,14−20] dedicated to developing AEMs with alkaline resiliency in base baths at elevated temperatures, as well as a plethora of reports on catalyst research in an alkaline medium,[16,21] a neglected area of materials research for AEMFCs and AEMWEs is the understanding of how AEIs interact with electrode and

Received: May 20, 2019
Accepted: September 3, 2019
Published: September 3, 2019

DOI: 10.1021/acsmaterialslett.9b00173
ACS Materials Lett. 2019, 1, 467−475

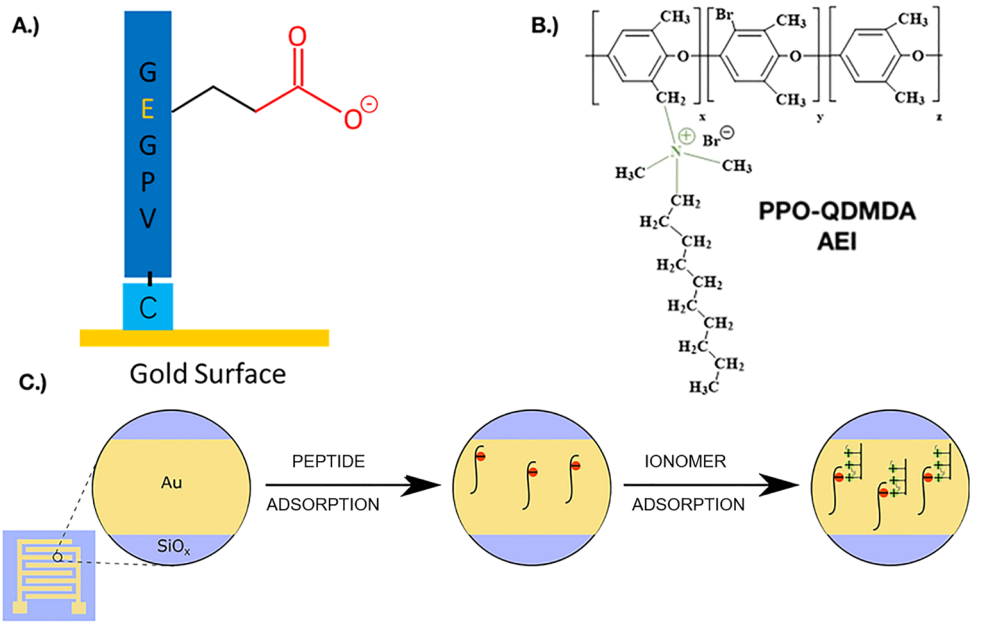

Figure 1. Process of using peptides to assemble AEI layers onto substrates. (A) Amino acid sequence of thiol-terminated elastin-like peptides bound to gold with a detailed view of the negatively charged guest residue (E) functional group. (B) Chemical structure of PPO-QDMDA AEI added to the substrate surfaces. (C) Process for peptide and/or AEI deposition on to IDEs (identical process used for gold QCM/coated wafers or SiOx wafers).

electrocatalyst surfaces.[1,22,23] These interactions have strong implications for ion conductivity in electrode layers, in addition to influencing reactant delivery and product removal to electrode surfaces[24,25] and charge-transfer reactions.[26−28] With respect to AEM-based fuel cells and electrolyzers, the breakthrough in peak power density of AEMFCs over 1 W cm^{-2} with hydrogen and oxygen (or over 0.8 W cm^{-2} with clean air) are ascribed to several factors that include new AEIs in the electrode layers (e.g., ETFE-AEI powders).[29−31] Hence, electrode ionomers have a profound impact on fuel cell and electrolyzer performance and stability, and thus serves as motivation for this work.[32] Some unanswered questions in the field, which we address in this study, include: how do the surfaces of electrodes impact AEI microstructure configurations? And as a result, how do the different microstructure configurations of AEIs in electrode layers, which may be different than bulk membrane materials, govern ionic conductivity?

This work reports the microstructure and ionic conductivity of an AEI model material, as a thin film, interfaced with a model electrode material (i.e., gold) with and without peptide modification and when processed via solvent vapor annealing. Previous studies by Renner and co-workers[33] have shown that sequence-defined bound peptides can alter interactions and microstructure arrangements of Nafion with electrode surfaces. While other surface modifications have been used to control the interactions with co-polymers (e.g. polymer brushes),[34] peptides are an attractive option, because they are easily tunable and possess well-defined secondary structures. Work done by Arges and co-workers[35,36] has shown that solvent vapor annealing facilitates microphase separation between ionic and nonionic domains in diblock, anion conducting copolymer electrolytes. Solvent vapor annealing lowers the glass transition of the polymer film below room temperature through solvent plasticization. The plasticized film becomes a

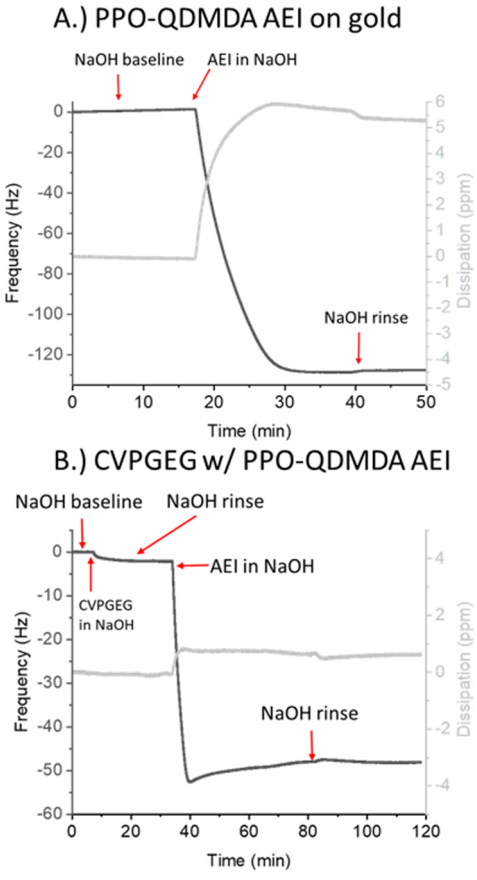

Figure 2. QCM-D experiments monitoring frequency (black) and dissipation (gray) shifts versus time for (A) PPO-QDMDA AEI adsorption onto a gold-coated sensor and (B) CVPGEG peptide adsorption, followed by PPO-QDMDA AEI adsorption onto a gold-coated sensor. The third overtone is shown.

DOI: 10.1021/acsmaterialslett.9b00173
ACS Materials Lett. 2019, 1, 467−475

polymer melt, and it can now diffuse and reorganize itself into a thermodynamically favorable microstructure.[37]

The overall goal of this study is to characterize the effect of biomolecular surface modifications with and without solvent annealing on the microstructure configurations of AEIs and subsequent ionic conductivity. The model AEI in this report is a random copolymer brush of poly(2,6-dimethyl 1,4-phenylene oxide) featuring quaternary benzyl *N*,*N*-dimethyl-*n*-decyl ammonium hydroxide/carbonate/bicarbonate anions (PPO-QDMDA). This material was selected because of its ease of preparation from commercially available polymers[38,39] and its ability to microphase-separate, because of the hydrophobic brush tails in the *N*,*N*-dimethyl-*n*-decyl ammonium moiety.[40,41] In addition, this class of PPO AEMs with alkyl brush tails has reasonable alkaline stability at 60 °C. Our work herein highlights thiol-terminated peptides, featuring anionic moieties, anchored to electrode and substrate surfaces that generate favorable microphase-separated grains in the PPO-based AEI. The results demonstrate the utility of both biomolecular modification and solvent vapor annealing for controlling the microphase separation of AEIs.

Table 1. Mass Loading, Estimated Thickness Values, and Viscoelastic Properties of AEI Films Calculated from QCM-D Data[a]

	Value	
	AEI on gold	AEI on peptide
mass loading (ng/cm^2)	3100 ± 700	1200 ± 300
thickness (nm)	30 ± 7	11 ± 2
viscosity (μPa s)	2800 ± 260	–
elastic modulus (kPa)	14 ± 5	–

[a]Values reported are the average, and the errors represent the standard error of parameters calculated from three separate QCM trials (n = 3).

Table 2. Film Thickness Results from Ellipsometry[a]

	Value	
	AEI without peptide	AEI with peptide
film thickness on silica substrate (nm)		
not annealed	21 ± 1	22 ± 2
solvent-annealed	23 ± 1	22 ± 1
film thickness on gold-coated wafer substrate (nm)		
not annealed	27 ± 6	18 ± 1
solvent-annealed	26 ± 8	27 ± 4

[a]Errors are the absolute difference from the average (n = 2).

Table 3. In-Plane Resistance and Ionic Conductivity (κ) Values of AEIs on IDE Substrates[a]

	Value	
	AEI with peptide	AEI with no peptide
not annealed		
R_1 (kΩ)	18 ± 7	52 ± 9
κ (mS cm^{-1})	32 ± 12	10 ± 2
solvent-annealed		
R_1 (kΩ)	46 ± 8	24 ± 8
κ (mS cm^{-1})	10 ± 2	22 ± 7

[a]Thickness value used for ionic conductivity determination came from ellipsometry experiments (data reported in Table 2). Error bars are the standard error for n = 3 independent samples.

Figure 1 depicts the sequence-defined thiol-terminated elastin-like peptide (CVPGEG) and the PPO-QDMDA AEI in addition to showing the surface adsorption procedure on to interdigitated electrode (IDE) substrates. This adsorption process was identical for gold and SiOx (i.e., silicon wafer with a 1-μm-thick thermally grown oxide layer) substrates. The terminal thiol group in CVPGEG binds to the gold forming a monolayer on the surface. Excess rinsing with dilute alkaline solutions rinsed away the nongrafted peptide. The diluted AEI then was deposited onto the aforementioned substrates with and without the grafted CVPGEG peptides.

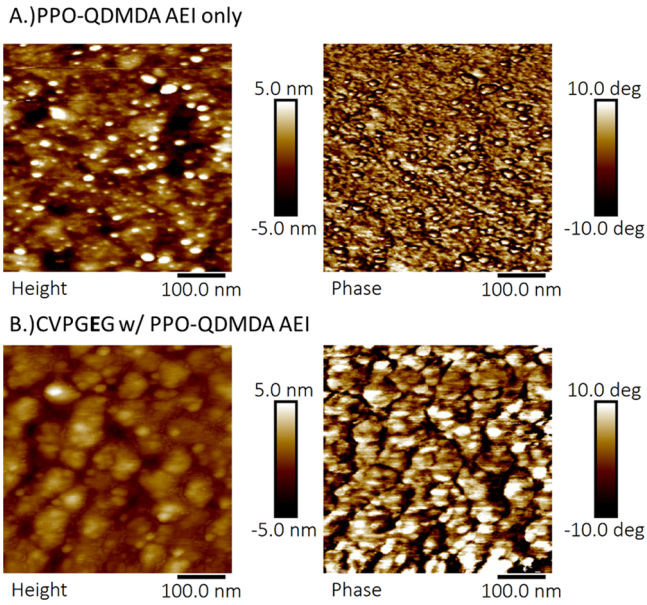

Figure 3. AFM micrographs of (A) height (left) and phase (right) images of PPO-QDMDA AEI on gold substrates; (B) height (left) and phase (right) images of CVPGEG peptide on gold substrate with PPO-QDMDA AEI assembled on top.

To characterize the adsorption phenomena of CVPGEG and PPO-QDMDA AEI to gold, QCM-D was used to sense the mass uptake and the retention of the deposited layers on a gold-coated AT cut quartz crystal. Figure 2 presents the shift in frequency and dissipation from QCM-D experiments that examined AEI adsorption in the presence (or absence) of surface-bound CVPGEG peptide. The negative frequency shift corresponds to the sensor gaining mass. The baseline solution and carrier, for all components tested, was dilute aqueous sodium hydroxide (NaOH). Figure 2A shows a representative experiment where a gold-coated sensor without peptide is exposed to an AEI solution, and Figure 2B shows a representative experiment where a gold-coated sensor with peptide is exposed to the AEI solution. Both samples experience negative frequency shifts in the presence of AEI, indicating the formation of an AEI layer. Generally, the AEI assembled on the bare gold electrode had large shifts in dissipation and was modeled as a viscoelastic film[42] (goodness of fit of >0.9, on average), whereas the AEI assembled on the peptide has small dissipation shifts and did not fit the viscoelastic model (goodness of fit of 0.4, on average). Details on the modeling can be found in the Methods section of the

DOI: 10.1021/acsmaterialslett.9b00173
ACS Materials Lett. 2019, 1, 467−475

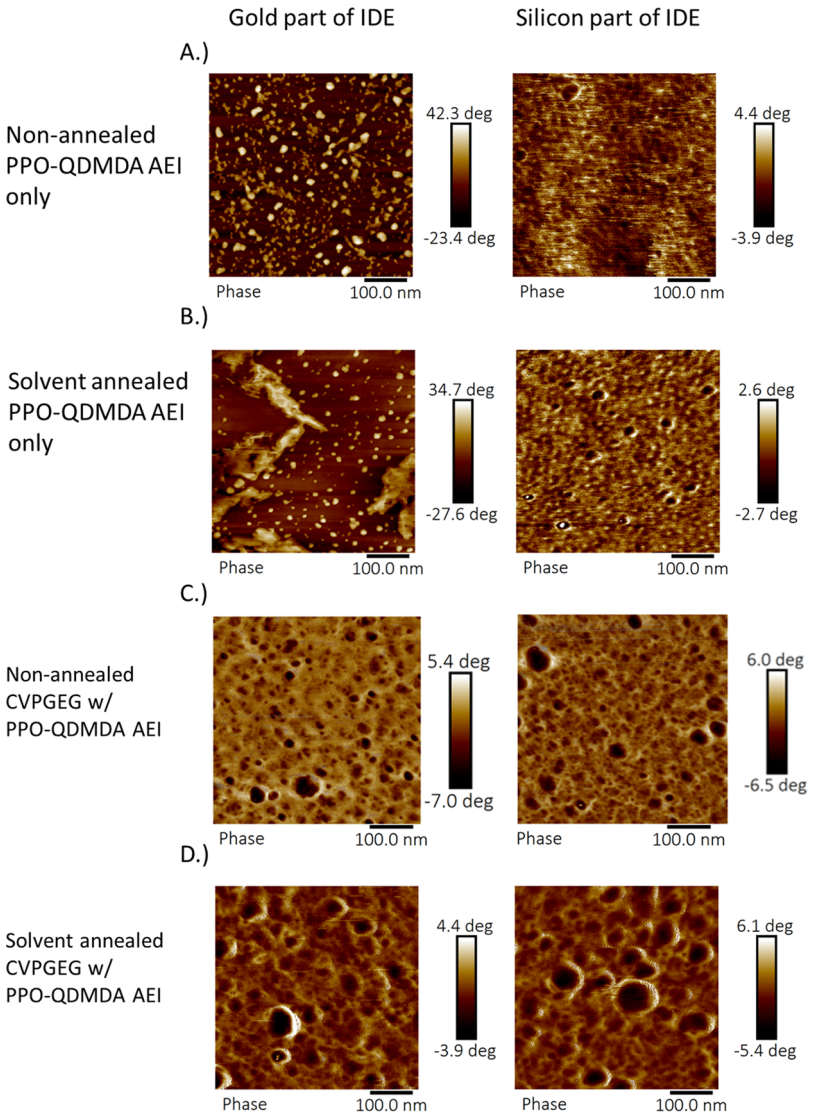

Figure 4. AFM micrographs of (A) PPO-QDMDA AEI layer, non-annealed, (B) PPO-QDMDA AEI layer, solvent annealed, (C) PPO-QDMDA AEI layer on CVPGEG peptide, and (D) PPO-QDMDA AEI layer on CVPGEG peptide and solvent-annealed. Left images are the AEI on the gold part of the IDE, and the right images are the AEI on the silica part of the IDE.

Supporting Information. This implies that the AEI film formed on the substrate with bound peptide had a different structure and is more rigid than the AEI film formed on gold without the peptide. The final rinse steps showed minimal frequency reverse or dissipation change over time. This indicated that the deposited peptide and AEI films were stable on the gold-based QCM substrate. Figure S1 in the Supporting Information provides the changes in frequency and dissipation versus time for all experiments, including repeats and Figure S2 in the Supporting Information summarizes the frequency and dissipation shifts, on average, for the final assembled AEI layers on gold versus bound peptide. Table 1 summarizes the mass uptake, AEI film thickness, and AEI viscoelastic properties estimated from the QCM-D data (see the Supporting Information for details about the modeling to obtain these values). Note that the AEI film thicknesses reported from QCM-D data do not include the peptide layer, which was estimated to be <1 nm.

Table 2 reports the film thickness values of the AEI adsorbed onto gold and silica substrates with and without a peptide layer from ellipsometry. Furthermore, this table contains film thickness values for samples that underwent solvent vapor annealing with 2-butanone. [Note: 2-butanone liquid was observed to solubilize PPO-QDMDA at 50 mg mL^{-1}.] The QCM-D results showed variation in film thickness for the AEI on the gold QCM substrates with and without peptide (range of 11−30 nm). Film thickness results by ellipsometry on silica substrates were more precise (within a range of 21−23 nm). However, the film thickness values by ellipsometry of the AEI on gold-coated wafers displayed a larger range (18−27 nm). It is important to note that the QCM-D measurements are made in a liquid flow environment, whereas the ellipsometry measurements are done in ambient air post-adsorption and solvent vapor annealing (if applicable). Despite the variances between the two independent methods, the thickness values were fairly close. Generally, the AEI/peptide−AEI films have a thickness value in the range of 10−30 nm on gold substrates. The adsorbed layers were ∼20 nm in thickness, on average, on silica substrates.

The QCM-D results substantiate that the peptide layer and AEI adsorbed to the gold substrates, while the ellipsometry results demonstrate peptide and AEI adsorption to both gold

DOI: 10.1021/acsmaterialslett.9b00173
ACS Materials Lett. 2019, 1, 467−475

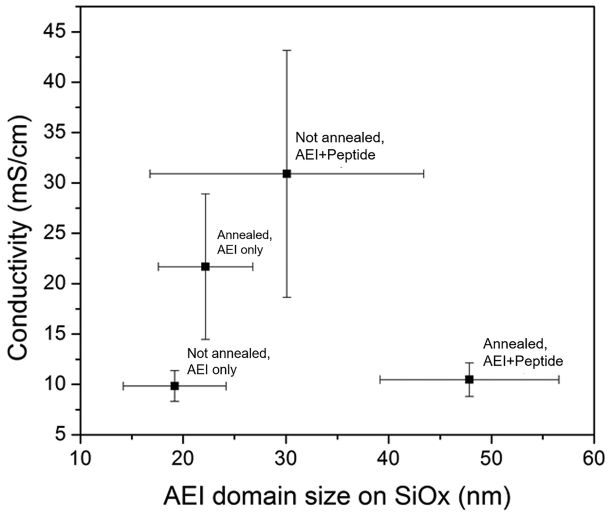

Figure 5. Ionic conductivity versus AEI ionic domain size on the SiOx region of the IDE. The *y*-axis error bars represent the standard error while the *x*-axis error bars correspond to the range of ionic grain sizes seen in the right column of Figure 4.

and silica substrates. The peptide adsorption is attributed to the thiol moiety in the terminal cysteine group, which binds to the gold[43] and silica surfaces.[44] The AEI adsorption to peptide-containing substrates partially arises from the quaternary ammonium moieties along the PPO backbone forming electrostatic interactions with the glutamate (E) residue (i.e., a carboxylate moiety) in the peptide chain. The electrostatic interactions anchor the AEI to the peptide that is bound to the substrate surface. Figure S3 in the Supporting Information verified the electrostatic interactions between the peptide CVPGEG and PPO-QDMDA AEI in liquid solution using dynamic light scattering (DLS). For the substrates not containing the peptide, the quaternary ammonium groups are also known to adsorb to gold[45] and silica.[46] The role of electrostatic interactions in AEI assembly on bare gold and peptide-functionalized gold was further confirmed by performing QCM-D in 10 mM sulfuric acid (see Figure S4 in the Supporting Information), where much lower frequency shifts were observed in both cases. The deposition process of peptides and AEI through immersion in dilute NaOH solutions was shown to be successful for the preparation of thin AEI films on electrode-type substrates. These thin films mimic the ionomer layers observed in the electrodes of fuel cells and electrolyzers.

After successful confirmation of the adsorption of AEI layers to bare and peptide-modified gold electrode surfaces, the in-plane ionic conductivity of the AEI films on IDEs were investigated using galvanostatic electrochemical impedance spectroscopy (EIS). The IDE substrates consisted of gold electrode teeth on silicon wafer substrates that contained a 1-μm-thick electron-insulating thermally grown silica layer (i.e., silica substrate). The IDE material composition was selected due to our previous observations that the AEI adsorbed to both gold and silica. Figure S5A in the Supporting Information shows representative Nyquist plots from EIS with the AEI samples covered in a drop of liquid deionized water. The impedance behavior of four different types of samples is plotted in Figure S5A: (i) AEI with peptide and no solvent vapor annealing, (ii) AEI without peptide and no solvent vapor annealing, (iii) AEI with peptide and solvent vapor annealing, and (iv) AEI without peptide and no solvent vapor annealing. The diameters of the semicircles in Figure S5A correspond to the in-plane resistance of the samples from ionic conduction within the AEI layer. Reports by Karan and co-workers, Patel and co-workers, and others, have shown that the semicircle diameter corresponds to ionic migration resistance.[47−53] Figure S5B in the Supporting Information is the electric circuit equivalent (ECE) model used to fit the data in the Nyquist plot to extract the in-plane resistance attributed to ionic conductance. Table 3 provides the modeled in-plane resistance values of the AEI samples, and it also reports the calculated in-plane ionic conductivity from the resistance values (see the Supporting Information). Equation S1 relates the in-plane ionic conductivity to the measured thickness values from ellipsometry, the IDE geometry, and the measured in-plane resistance. The samples with the AEI film assembled on a peptide layer, but not solvent-annealed, displayed one of the highest ionic conductivity values (32 ± 12 mS cm^{-1}). A statistically equivalent ionic conductivity value was attained (22 ± 7 mS cm^{-1}) with AEI without peptide, but solvent-annealed. Conversely, the AEI film without peptide or solvent vapor annealing yielded a significantly lower ionic conductivity value of (10 ± 2 mS cm^{-1}). The AEI film with peptide and that was solvent-annealed displayed a similarly low ionic conductivity value (10 ± 2 mS cm^{-1}) to the AEI without the peptide sample but not solvent-annealed.

The results reported in Table 3 highlight that peptide modified electrodes and solvent vapor annealing are extremely influential on the ionic conductivity of AEIs. For the AEI with the peptide-modified electrode that was not solvent-annealed, the gain in ionic conductivity cannot be taken into account by the carboxylate moieties in the peptide. The peptide features a low ion-exchange capacity value (1.66 mmol g^{-1}) and thus it lacks the quantity of fixed-charge carriers to augment the ionic conductivity. Second, the carboxylate group binds a small fraction of the quaternary ammonium groups in the PPO-QDMDA AEI and the rinse step will wash away the released HCl from the adsorption process (i.e., hydronium comes from the peptide and the chloride counterion comes from the quaternary ammonium in PPO-QDMDA). Because the number of carboxylate groups is smaller, compared to the AEI, it is assumed that all the hydronium counterions are removed. Hence, this also explains why the peptide layer cannot contribute to the ionic conductivity. It can only bind the AEI through electrostatic interactions, as verified by Figure S3 via DLS. To understand why the peptide and solvent vapor annealing processing impacted the ionic conductivity of the AEI thin films, the microstructures of the AEI samples were investigated by tapping-mode AFM.

Figures 3A and 3B present the AFM topography and phase images of the AEI films on the QCM gold substrates with and without a peptide layer. The AEI layer deposited on the gold QCM sensor without a peptide displayed smaller phase-separated grains (light circles in phase image) when compared with the phase images of AEI assembled on a peptide layer (Figure 3B). The sample with AEI assembled on gold without peptide produced grains that were 14 ± 1 nm in size, versus the sample with AEI assembled on peptide, which produced grains that were 31 ± 2 nm. Interestingly, the AEI sample with the peptide underneath showed more uniformity in the AFM height images, when compared to the AEI on gold by itself. Recall that the QCM results indicated that there was more AEI mass uptake during the adsorption process for the electrode

DOI: 10.1021/acsmaterialslett.9b00173
ACS Materials Lett. 2019, 1, 467−475

without the peptide. Hence, the mass uptake data and AFM height image in Figure 3A indicate that more mass uptake does not necessarily result in more uniform deposition of the AEI layer. Figures 3A and 3B clearly show that the film uniformity and grain microstructure for the AEI differ if a peptide is present on the gold surface. Overall, the AFM images reveal why the AEI with the peptide underneath may yield higher ionic conductivity. However, it is important to note that the IDE substrates contain gold electrodes and a silica layer between the gold electrodes. The difference in the IDE samples could cause varying microstructures, and thus the microstructures of the AEI on the IDEs were interrogated by AFM.

Figures 4A−D present the AFM phase images of AEI microstructures on IDEs in the areas with gold electrodes and the areas with the silica substrate. Figure 4A is the assembled AEI sample with no peptide and was not solvent-annealed, and Figure 4B is the assembled AEI sample with no peptide that was solvent-annealed. Figure 4C represents the AEI sample assembled on peptide without solvent annealing, and Figure 4D is the AEI assembled on a peptide layer that was solvent-annealed with 2-butanone. It is assumed the dark spots in most of the phase images for Figure 4 correspond to the ionic domains. It is clear from the AFM images in the silica regions of the IDE that the AEI by itself appear to have the smallest microphase-separated ionic grains (18−24 nm in size), while the AEI with the peptide and the AEI by itself but solvent-annealed have slightly larger ionic grains (20−35 nm in size). Recall that the AEI assembled with a peptide, but not annealed, and the AEI by itself, but annealed, displayed roughly a two- to three-fold increase in ionic conductivity over the AEI by itself and not annealed. The substantial increase in ionic conductivity for the samples in Figures 4B and 4C are attributed to their larger ionic grains in the silica regions of the IDEs. It is clear that the increase in ionic grains, spurred by the peptide-modified electrodes and solvent vapor annealing, resulted in higher ionic conductivity. However, this trend has limitations. The AFM phase image of the assembled AEI on a peptide layer and solvent-annealed (Figure 4D) displayed excessively large ionic grains of 30−65 nm. This sample was observed to have low ionic conductivity that is similar to the AEI by itself and was not annealed. Hence, appropriately sized ionic grains afforded the best ionic conductivity for thin-film PPO-QDMDA AEI samples (see Figure 5).

To probe the effect of solvent vapor annealing on the peptide structure itself, Fourier-transform infrared spectroscopy (FTIR) measurements were taken on gold QCM sensors with an assembled peptide layer. A sample exposed to DI water was compared to a sample exposed to 2-butanone, which was the same solvent used in vapor annealing. The results shown in Figure S6 feature a peak at ∼1675 cm^{-1} in both samples, which was observed previously with a similar peptide,[33] and suggests that a β-turn structure is present even after exposure to 2-butanone. Similarly, Thomas et al.[54] observed the preservation of secondary structure in larger proteins after exposure to solvent vapor annealing. These data indicate that the differences in microphase structure observed are not due to structural modifications in the peptide.

The AEI on the gold portion of the IDEs showed different coverage and microphase behavior than the AEI in the silica regions if no peptide was applied to the substrate (Figures 4A and 4B). Conversely, the peptide modified electrodes caused the AEI to yield the same coverage uniformity and microstructure arrangement for samples that are (or are not) solvent-annealed (see Figures 4C and 4D). These images provide further evidence explaining why the AEI on the peptide layer that was not annealed displayed the highest ionic conductivity, on average: (i) the sample had appropriately sized ionic domains and (ii) the AEI was uniformly covered on the gold and silica portion of the IDEs. Figures S7A−7E in the Supporting Information present Raman spectra and maps of the peptide on the IDE before addition of AEI. These results substantiated uniform coverage of the peptide over the IDE leading to uniform AEI microstructure across the IDE. Recall that the AFM images of AEI on gold QCM sensors (Figures 3A and 3B) also substantiated that the AEI had better coverage and larger grains when the gold was modified with an adsorbed peptide. It is important to note that the morphologies of the AEI on the gold QCM sensors were different than the gold portion of the IDEs. This may be due to the gold surfaces being different: the gold on IDEs is ∼2 times rougher, in comparison to the gold on QCM-D sensors, according to AFM topography images (images and roughness factors shown in Figure S8 in the Supporting Information). We also speculate that the difference in gold surface roughness is the reason why the grains are sometimes represented by a different color (light vs dark) in Figures 3 and 4, since topography has been shown to affect phase imaging.[55]

Figure 5 summarizes the trends between ionic conductivity and the sized ionic domains. Although Figure 5 suggests that an optimal ionic grain size may give the best ionic conductivity for PPO-QDMDA (a 2- to 3-fold improvement over the lowest value attained), it is important to note that other reports highlight that smaller ionic domains give higher ionic conductivity[56,57] or ionic grain size does not impact ionic conductivity at all.[58] The difficulty in correlating ionic grain size to ionic conductivity relates to the control of other structural factors such as percolation and tortuosity.[36,59] The work here is the starting point to manipulate microstructures of AEIs with peptides and solvent vapor annealing. Other AEI systems, such as block copolymers, that are more conducive to long-range order and connectivity[59] will be pursued in future studies with modified electrode surfaces to definitively understand how grain size impacts ionic conductivity.

Sequence-defined peptides, featuring a carboxylate moiety, anchored to a surface generated better ionomer coverage and larger microphase-separated ionic grains compared to samples with AEI films assembled without the peptides. In turn, the appropriately sized ionic grains that formed on the peptide layer substantially improved thin-film ionic conductivity by a factor of three, compared to samples without peptide. When the samples were solvent-vapor-annealed, appropriately sized ionic grains were observed in the microphase-separated PPO-QDMDA AEI assembled without a peptide, but nonuniform coverage persisted. Lastly, a combination of peptide-modified electrodes and solvent vapor annealing resulted in large AEI ionic domains that were as large as 65 nm, but the larger domains proved catastrophic to AEI conductivity. Generally, these results show that both biomolecular modifications and solvent vapor annealing can be used to control the microphase separation of AEIs on solid surfaces to discover important structure-property information, such as ideal grain size for ionic conductivity. Future work will take advantage of this discovery by exploring the rich design space enabled by different peptide sequences in combination with different solvent vapor annealing conditions, AEI block copolymer

DOI: 10.1021/acsmaterialslett.9b00173
ACS Materials Lett. 2019, 1, 467−475

designs, and electrode potential to achieve new microphase-separated structures and to investigate their functional properties.

■ ASSOCIATED CONTENT

Supporting Information

The Supporting Information is available free of charge on the ACS Publications website at DOI: 10.1021/acsmaterialslett.9b00173.

List of materials used to prepare samples, the synthesis procedures for the thiol-terminated peptides and PPO-QDMDA AEI, and the manufacturing procedure for IDEs via photolithography; methods for dynamic light scattering, surface Raman mapping, FTIR, QCM-D, peptide and AEI adsorption to substrate surfaces, solvent vapor annealing, EIS, and AFM experiments (PDF)

■ AUTHOR INFORMATION

Corresponding Authors

*E-mail: jxr484@case.edu (J. N. Renner).
*E-mail: carges@lsu.edu (C. G. Arges).

ORCID

Zihang Su: 0000-0001-6216-6880
Varada M. Palakkal: 0000-0003-0904-0298
Christopher G. Arges: 0000-0003-1703-8323

Author Contributions

▽These authors contributed equally to this work.

Notes

The authors declare no competing financial interest.

■ ACKNOWLEDGMENTS

This work by C.G.A. and his laboratory was supported by the National Science Foundation (Award No. 1703307). He also acknowledges the LSU Nanofabrication Facility for preparing the IDEs, the LSU Shared Instrumentation Facility (SIF) for use of the Renishaw in Via Reflex Raman Spectroscope, and Mr. Daniel Willis for assisting us in thermal evaporation of titanium and gold for the preparation of IDEs. C.G.A. also thanks Mr. Deepra Bhattacharya for helping prepare Figure 1. The work performed by J.N.R. and her laboratory was supported by the United States Department of Agriculture (Award No. 2018-68011-28691). J.N.R. also appreciates support from an NSF-sponsored Research Experiences for Undergraduates Award (No. 1659394). We thank the Swagelok Center for Surface Analysis of Materials located at CWRU for their work in helping obtain AFM data, and the Protein Expression Purification Crystallization and Molecular Biophysics Core at CWRU for assistance with DLS measurements.

■ REFERENCES

(1) Arges, C. G.; Zhang, L. Anion Exchange Membranes' Evolution toward High Hydroxide Ion Conductivity and Alkaline Resiliency. *ACS Appl. Energy Mater.* **2018**, *1*, 2991−3012.

(2) Varcoe, J. R.; Atanassov, P.; Dekel, D. R.; Herring, A. M.; Hickner, M. A.; Kohl, P. A.; Kucernak, A. R.; Mustain, W. E.; Nijmeijer, K.; Scott, K.; Xu, T.; Zhuang, L. Anion-exchange membranes in electrochemical energy systems. *Energy Environ. Sci.* **2014**, *7*, 3135−3191.

(3) Parrondo, J.; Arges, C. G.; Niedzwiecki, M.; Anderson, E. B.; Ayers, K. E.; Ramani, V. Degradation of anion exchange membranes used for hydrogen production by ultrapure water electrolysis. *RSC Adv.* **2014**, *4*, 9875−9879.

(4) Parrondo, J.; George, M.; Capuano, C.; Ayers, K. E.; Ramani, V. Pyrochlore electrocatalysts for efficient alkaline water electrolysis. *J. Mater. Chem. A* **2015**, *3*, 10819−10828.

(5) Ayers, K. E.; Parrondo, J.; Capuano, C.; George, M.; Ramani, V. K.; Fujimoto, C. *Current State of the Art in Water Electrolysis Performance Based on Anion Exchange Membranes*. Presented at the *228th Electrochemical Society Meeting*, Phoenix, AZ, USA, 2015.

(6) Xiao, L.; Zhang, S.; Pan, J.; Yang, C.; He, M.; Zhuang, L.; Lu, J. First implementation of alkaline polymer electrolyte water electrolysis working only with pure water. *Energy Environ. Sci.* **2012**, *5*, 7869−7871.

(7) Marcinkoski, J.; Spendelow, J.; Wilson, A.; Papageorgopoulos, D. *Fuel Cell System Cost—2015*; U.S. DOE Hydrogen and Fuel Cells Program Record, 2015; pp 1−9.

(8) Kongkanand, A.; Mathias, M. F. The Priority and Challenge of High-Power Performance of Low-Platinum Proton-Exchange Membrane Fuel Cells. *J. Phys. Chem. Lett.* **2016**, *7*, 1127−1137.

(9) Ayers, K. E.; Renner, J. N.; Danilovic, N.; Wang, J. X.; Zhang, Y.; Maric, R.; Yu, H. Pathways to ultra-low platinum group metal catalyst loading in proton exchange membrane electrolyzers. *Catal. Today* **2016**, *262*, 121−132.

(10) McLean, G. F.; Niet, T.; Prince-Richard, S.; Djilali, N. An assessment of alkaline fuel cell technology. *Int. J. Hydrogen Energy* **2002**, *27*, 507−526.

(11) Schulze, M.; Gulzow, E. Degradation of nickel anodes in alkaline fuel cells. *J. Power Sources* **2004**, *127*, 252−263.

(12) Wagner, N.; Schulze, M.; Gulzow, E. Long term investigations of silver cathodes for alkaline fuel cells. *J. Power Sources* **2004**, *127*, 264−272.

(13) Arges, C. G.; Ramani, V.; Pintauro, P. N. The chalkboard: Anion exchange membrane fuel cells. *Electrochem. Soc. Interface* **2010**, *19*, 31−35.

(14) Dekel, D. R. Review of cell performance of anion exchange membrane fuel cells. *J. Power Sources* **2018**, *375*, 158.

(15) Gottesfeld, S.; Dekel, D. R.; Page, M.; Bae, C.; Yan, Y.; Zelenay, P.; Kim, Y. S. Anion exchange membrane fuel cells: Current status and remaining challenges. *J. Power Sources* **2018**, *375*, 170−184.

(16) Serov, A.; Zenyuk, I. V.; Arges, C. G.; Chatenet, M. Hot topics in alkaline exchange membrane fuel cells. *J. Power Sources* **2018**, *375*, 149−157.

(17) Varcoe, J. R.; Slade, R. C. T. Prospects for alkaline anion-exchange membranes in low temperature fuel cells. *Fuel Cells (Weinheim, Ger.)* **2005**, *5*, 187−200.

(18) Jannasch, P.; Weiber, E. A. Configuring Anion-Exchange Membranes for High Conductivity and Alkaline Stability by Using Cationic Polymers with Tailored Side Chains. *Macromol. Chem. Phys.* **2016**, *217*, 1108−1118.

(19) Merle, G.; Wessling, M.; Nijmeijer, K. Anion exchange membranes for alkaline fuel cells: A review. *J. Membr. Sci.* **2011**, *377*, 1−35.

(20) Couture, G.; Alaaeddine, A.; Boschet, F.; Ameduri, B. Polymeric materials as anion-exchange membranes for alkaline fuel cells. *Prog. Polym. Sci.* **2011**, *36*, 1521−1557.

(21) Lafforgue, C.; Zadick, A.; Dubau, L.; Maillard, F.; Chatenet, M. Selected Review of the Degradation of Pt and Pd-based Carbon-supported Electrocatalysts for Alkaline Fuel Cells: Towards Mechanisms of Degradation. *Fuel Cells (Weinheim, Ger.)* **2018**, *18*, 229−238.

(22) Higgins, D. C.; Hahn, C.; Xiang, C.; Jaramillo, T. F.; Weber, A. Z. Gas-Diffusion Electrodes for Carbon-Dioxide Reduction: A New Paradigm. *ACS Energy Lett.* **2019**, *4*, 317.

(23) Abbasi, R.; Setzler, B. P.; Lin, S.; Wang, J.; Zhao, Y.; Xu, H.; Pivovar, B.; Tian, B.; Chen, X.; Wu, G.; Yan, Y. A Roadmap to Low-Cost Hydrogen with Hydroxide Exchange Membrane Electrolyzer. *Adv. Mater.* **2019**, *31*, 1805876.

DOI: 10.1021/acsmaterialslett.9b00173
ACS Materials Lett. 2019, 1, 467−475

(24) Sambandam, S.; Ramani, V. Influence of binder properties on kinetic and transport processes in polymer electrolyte fuel cell electrodes. *Phys. Chem. Chem. Phys.* **2010**, *12*, 6140−6149.
(25) Kim, D. S.; Fujimoto, C. H.; Hibbs, M. R.; Labouriau, A.; Choe, Y.-K.; Kim, Y. S. Resonance Stabilized Perfluorinated Ionomers for Alkaline Membrane Fuel Cells. *Macromolecules (Washington, DC, U. S.)* **2013**, *46*, 7826−7833.
(26) Subbaraman, R.; Strmcnik, D.; Paulikas, A. P.; Stamenkovic, V. R.; Markovic, N. M. Oxygen Reduction Reaction at Three-Phase Interfaces. *ChemPhysChem* **2010**, *11*, 2825−2833.
(27) Subbaraman, R.; Strmcnik, D.; Stamenkovic, V.; Markovic, N. M. Three Phase Interfaces at Electrified Metal-Solid Electrolyte Systems 1. Study of the Pt(hkl)-Nafion Interface. *J. Phys. Chem. C* **2010**, *114*, 8414−8422.
(28) Li, D.; Chung, H. T.; Maurya, S.; Matanovic, I.; Kim, Y. S. Impact of ionomer adsorption on alkaline hydrogen oxidation activity and fuel cell performance. *Curr. Opin. Electrochem.* **2018**, *12*, 189−195.
(29) Omasta, T. J.; Zhang, Y.; Park, A. M.; Peng, X.; Pivovar, B.; Varcoe, J. R.; Mustain, W. E. Strategies for Reducing the PGM Loading in High Power AEMFC Anodes. *J. Electrochem. Soc.* **2018**, *165*, F710−F717.
(30) Omasta, T. J.; Park, A. M.; La Manna, J. M.; Zhang, Y.; Peng, X.; Wang, L.; Jacobson, D. L.; Varcoe, J. R.; Hussey, D. S.; Pivovar, B. S.; Mustain, W. E. Beyond catalysis and membranes: visualizing and solving the challenge of electrode water accumulation and flooding in AEMFCs. *Energy Environ. Sci.* **2018**, *11*, 551−558.
(31) Wang, J.; Zhao, Y.; Setzler, B. P.; Rojas-Carbonell, S.; Ben Yehuda, C.; Amel, A.; Page, M.; Wang, L.; Hu, K.; Shi, L.; Gottesfeld, S.; Xu, B.; Yan, Y. Poly(aryl piperidinium) membranes and ionomers for hydroxide exchange membrane fuel cells. *Nat. Energy* **2019**, *4*, 392.
(32) Kusoglu, A.; Weber, A. Z. New Insights into Perfluorinated Sulfonic-Acid Ionomers. *Chem. Rev.* **2017**, *117*, 987−1104.
(33) Su, Z.; Pramounmat, N.; Watson, S. T.; Renner, J. N. Engineered interaction between short elastin-like peptides and perfluorinated sulfonic-acid ionomer. *Soft Matter* **2018**, *14*, 3528−3535.
(34) Mansky, P.; Liu, Y.; Huang, E.; Russell, T. P.; Hawker, C. Controlling Polymer-Surface Interactions with Random Copolymer Brushes. *Science* **1997**, *275*, 1458.
(35) Arges, C. G.; Kambe, Y.; Suh, H. S.; Ocola, L. E.; Nealey, P. F. Perpendicularly Aligned, Anion Conducting Nanochannels in Block Copolymer Electrolyte Films. *Chem. Mater.* **2016**, *28*, 1377−1389.
(36) Arges, C. G.; Kambe, Y.; Dolejsi, M.; Wu, G.-P.; Segal-Pertz, T.; Ren, J.; Cao, C.; Craig, G. S. W.; Nealey, P. F. Interconnected ionic domains enhance conductivity in microphase separated block copolymer electrolytes. *J. Mater. Chem. A* **2017**, *5*, 5619−5629.
(37) Xiong, S.; Li, D.; Hur, S.-M.; Craig, G. S. W.; Arges, C. G.; Qu, X.-P.; Nealey, P. F. The Solvent Distribution Effect on the Self-Assembly of Symmetric Triblock Copolymers during Solvent Vapor Annealing. *Macromolecules (Washington, DC, U. S.)* **2018**, *51*, 7145−7151.
(38) Arges, C.; Wang, L.; Parrondo, J.; Ramani, V. Best Practices for Investigating Anion Exchange Membrane Suitability for Alkaline Electrochemical Devices: Case Study Using Quaternary Ammonium Poly(2,6-dimethyl 1,4-phenylene)oxide Anion Exchange Membranes. *J. Electrochem. Soc.* **2013**, *160*, F1258−F1274.
(39) Arges, C. G.; Wang, L.; Jung, M.-s.; Ramani, V. Mechanically Stable Poly(arylene ether) Anion Exchange Membranes Prepared from Commercially Available Polymers for Alkaline Electrochemical Devices. *J. Electrochem. Soc.* **2015**, *162*, F686−F693.
(40) Li, N.; Yan, T.; Li, Z.; Thurn-Albrecht, T.; Binder, W. H. Comb-shaped polymers to enhance hydroxide transport in anion exchange membranes. *Energy Environ. Sci.* **2012**, *5*, 7888−7892.
(41) Li, N.; Leng, Y.; Hickner, M. A.; Wang, C.-Y. Highly stable, anion conductive, comb-shaped copolymers for alkaline fuel cells. *J. Am. Chem. Soc.* **2013**, *135*, 10124−10133.
(42) Voinova, M. V.; Rodahl, M.; Jonson, M.; Kasemo, B. Viscoelastic Acoustic Response of Layered Polymer Films at Fluid-Solid Interfaces: Continuum Mechanics Approach. *Phys. Scr.* **1999**, *59*, 391−396.
(43) Castner, D. G.; Hinds, K.; Grainger, D. W. X-ray photoelectron spectroscopy sulfur 2p study of organic thiol and disulfide binding interactions with gold surfaces. *Langmuir* **1996**, *12*, 5083−5086.
(44) Quang, D. V.; Lee, J. E.; Kim, J.-K.; Kim, Y. N.; Shao, G. N.; Kim, H. T. A gentle method to graft thiol-functional groups onto silica gel for adsorption of silver ions and immobilization of silver nanoparticles. *Powder Technol.* **2013**, *235*, 221−227.
(45) Chen, S.; Liu, Y.; Wu, G. Stabilized and size-tunable gold nanoparticles formed in a quaternary ammonium-based room-temperature ionic liquid under γ-irradiation. *Nanotechnology* **2005**, *16*, 2360.
(46) Walcarius, A.; Ganesan, V. Ion-exchange properties and electrochemical characterization of quaternary ammonium-functionalized silica microspheres obtained by the surfactant template route. *Langmuir* **2006**, *22*, 469−477.
(47) Modestino, M. A.; Paul, D. K.; Dishari, S.; Petrina, S. A.; Allen, F. I.; Hickner, M. A.; Karan, K.; Segalman, R. A.; Weber, A. Z. Self-Assembly and Transport Limitations in Confined Nafion Films. *Macromolecules* **2013**, *46*, 867−873.
(48) Paul, D. K.; McCreery, R.; Karan, K. Proton Transport Property in Supported Nafion Nanothin Films by Electrochemical Impedance Spectroscopy. *J. Electrochem. Soc.* **2014**, *161*, F1395−F1402.
(49) Kusoglu, A.; Kushner, D.; Paul, D. K.; Karan, K.; Hickner, M. A.; Weber, A. Z. Impact of Substrate and Processing on Confinement of Nafion Thin Films. *Adv. Funct. Mater.* **2014**, *24*, 4763−4774.
(50) Sharon, D.; Bennington, P.; Liu, C.; Kambe, Y.; Dong, B. X.; Burnett, V. F.; Dolejsi, M.; Grocke, G.; Patel, S. N.; Nealey, P. F. Interrogation of electrochemical properties of polymer electrolyte thin films with interdigitated electrodes. *J. Electrochem. Soc.* **2018**, *165*, H1028−H1039.
(51) Arges, C. G.; Li, K.; Zhang, L.; Kambe, Y.; Wu, G.-P.; Lwoya, B.; Albert, J. N. L.; Nealey, P. F.; Kumar, R. Ionic conductivity and counterion condensation in nanoconfined polycation and polyanion brushes prepared from block copolymer templates. *Mol. Syst. Des. Eng.* **2019**, *4*, 365−378.
(52) Dong, B. X.; Bennington, P.; Kambe, Y.; Sharon, D.; Dolejsi, M.; Strzalka, J.; Burnett, V. F.; Nealey, P. F.; Patel, S. N. Nanothin film conductivity measurements reveal interfacial influence on ion transport in polymer electrolytes. *Mol. Syst. Des. Eng.* **2019**, *4*, 597.
(53) Dong, B. X.; Nowak, C.; Onorato, J. W.; Strzalka, J.; Escobedo, F. A.; Luscombe, C. K.; Nealey, P. F.; Patel, S. N. Influence of Side-Chain Chemistry on Structure and Ionic Conduction Characteristics of Polythiophene Derivatives: A Computational and Experimental Study. *Chem. Mater.* **2019**, *31*, 1418−1429.
(54) Thomas, C. S.; Xu, L.; Olsen, B. D. Kinetically Controlled Nanostructure Formation in Self-Assembled Globular Protein−Polymer Diblock Copolymers. *Biomacromolecules* **2012**, *13*, 2781−2792.
(55) YE, Z.; ZHAO, X. Phase imaging atomic force microscopy in the characterization of biomaterials. *J. Microsc.* **2010**, *238*, 27−35.
(56) Chintapalli, M.; Chen, X. C.; Thelen, J. L.; Teran, A. A.; Wang, X.; Garetz, B. A.; Balsara, N. P. Effect of Grain Size on the Ionic Conductivity of a Block Copolymer Electrolyte. *Macromolecules (Washington, DC, U. S.)* **2014**, *47*, 5424−5431.
(57) Chen, W.; Mandal, M.; Huang, G.; Wu, X.; He, G.; Kohl, P. A. Highly Conducting Anion-Exchange Membranes Based on Cross-Linked Poly(norbornene): Ring Opening Metathesis Polymerization. *ACS App. Energy Mater.* **2019**, *2*, 2458−2468.
(58) Sanoja, G. E.; Popere, B. C.; Beckingham, B. S.; Evans, C. M.; Lynd, N. A.; Segalman, R. A. Structure−Conductivity Relationships of Block Copolymer Membranes Based on Hydrated Protic Polymerized Ionic Liquids: Effect of Domain Spacing. *Macromolecules* **2016**, *49*, 2216.
(59) Kambe, Y.; Arges, C. G.; Czaplewski, D. A.; Dolejsi, M.; Krishnan, S.; Stoykovich, M. P.; de Pablo, J. J.; Nealey, P. F. Role of

DOI: 10.1021/acsmaterialslett.9b00173
ACS Materials Lett. 2019, 1, 467−475

Defects in Ion Transport in Block Copolymer Electrolytes. *Nano Lett.* **2019**, *19*, 4684.

DOI: 10.1021/acsmaterialslett.9b00173
ACS Materials Lett. 2019, 1, 467−475